Journal of Structural Biology 213 (2021) 107658

Contents lists available at ScienceDirect

Journal of Structural Biology

journal homepage: www.elsevier.com/locate/yjsbi

Movement analysis of primate molar teeth under load using synchrotron X-ray microtomography

Maximilian Bemmann [a,b], Ellen Schulz-Kornas [a,b,c], Jörg U. Hammel [d], Alexander Hipp [d], Julian Moosmann [d], Anthony Herrel [e], Alexander Rack [f], Ute Radespiel [g], Elke Zimmermann [g], Thomas M. Kaiser [c], Kornelius Kupczik [a,*]

[a] Max Planck Weizmann Center for Integrative Archaeology and Anthropology, Max-Planck-Institute for Evolutionary Anthropology, 04103 Leipzig, Germany
[b] Department of Cariology, Endodontics and Periodontology, University of Leipzig, Liebigstrasse 12, 04103 Leipzig, Germany
[c] Center of Natural History (CeNak), University of Hamburg, Hamburg, Germany
[d] Institute of Materials Research, Helmholtz-Zentrum Geesthacht, 21502 Geesthacht, Germany
[e] UMR 7179 C.N.R.S/M.N.H.N., Département Adaptations du Vivant, Bâtiment d'Anatomie Comparée, 55 rue Buffon, 75005 Paris, France
[f] ESRF The European Synchrotron, 71 Rue des Martyrs, 38000 Grenoble, France
[g] Institute of Zoology, University of Veterinary Medicine Hannover, Buenteweg 17, 30559 Hannover, Germany

ARTICLE INFO

Keywords:
3D movement
Biomechanics
Mouse lemur
Synchrotron
Tooth loading

ABSTRACT

Mammalian teeth have to sustain repetitive and high chewing loads without failure. Key to this capability is the periodontal ligament (PDL), a connective tissue containing a collagenous fibre network which connects the tooth roots to the alveolar bone socket and which allows the teeth to move when loaded. It has been suggested that rodent molars under load experience a screw-like downward motion but it remains unclear whether this movement also occurs in primates. Here we use synchroton micro-computed tomography paired with an axial loading setup to investigate the form-function relationship between tooth movement and the morphology of the PDL space in a non-human primate, the mouse lemur (*Microcebus murinus*). The loading behavior of both mandibular and maxillary molars showed a three-dimensional movement with translational and rotational components, which pushes the tooth into the alveolar socket. Moreover, we found a non-uniform PDL thickness distribution and a gradual increase in volumetric proportion of the periodontal vasculature from cervical to apical. Our results suggest that the PDL morphology may optimize the three-dimensional tooth movement to avoid high stresses under loading.

1. Introduction

Mammalian teeth are adapted to endure high and repetitive occlusal forces during mastication over an individual's lifetime without damage or loss of function. A key to this capability is that the teeth can move vertically and horizontally inside the alveolar bone socket when occlusally loaded. This so called physiological tooth movement is guided by the tooth roots that are connected to the alveolar bone socket by a fibrous, soft tissue known as the periodontal ligament or PDL, which is suggested to act as a suspensory mechanism under occlusal loads (Fig. 1) (Luke, 1992; Picton, 1990). The PDL is a composite tissue composed of different types of collagenous fibres, embedded in a protein rich water-based matrix, in addition to vasculature and connective tissue (McDonald, 2009; Nanci and Bosshardt, 2006). This type of tooth (root) attachment type is called gomphosis and found across mammals and their fossil (therapsid) ancestors, as well as in many archosaurs (including all dinosaurs and extant crocodilians) (LeBlanc et al., 2018; 2016). It is generally agreed that the PDL, as the softest component of the tooth bone complex, controls the tooth movement to dissipate physiological and non-physiological loads and is therefore vital to avoid non-repairable damage to the dental hard tissues or the alveolar bone (Lin et al., 2013; McDonald, 2009; Mühlemann, 1951; Storey, 1973). Moreover, *ex vivo* loading experiments have shown that in the case of tooth ankylosis, i.e. the pathological fusion of the tooth with the alveolar bone, mobility is significantly reduced (Chattah et al., 2009; Picton and Davies, 1967).

The mechanical response of teeth under load has been studied in both single- and multi-rooted teeth of humans (Behrend, 1978; Burstone

* Corresponding author.
E-mail address: Kornelius_kupczik@eva.mpg.de (K. Kupczik).

https://doi.org/10.1016/j.jsb.2020.107658
Received 29 June 2020; Received in revised form 19 October 2020; Accepted 20 October 2020
Available online 15 November 2020

et al., 1978; Jenatschke, 1975; Kawarizadeh et al., 2003; Manly et al., 1951; Miura et al., 1998; Mühlemann, 1951; Siebert, 1981), macaques (Wills et al., 1976), rats (Kawarizadeh et al., 2003; Naveh et al., 2012b; Naveh and Weiner, 2015), pigs (Salamati et al., 2020) and mini-pigs (Chattah et al., 2009). Tooth movement occurs under physiological occlusal loading during chewing (Behrend, 1978; Miura et al., 1998; Siebert, 1981) and is affected by different factors such as the morphology and number of tooth roots (Picton, 1963), pathological changes to the PDL (Persson, 1981) and changes to the structure and pressure of the blood vessel system (Slatter and Picton, 1972). The 3D movement of the tooth can be described spatially by three translations along and three rotations around the main axes, as has been shown for both single-rooted human incisors and multi-rooted rat molars (Burstone et al., 1978; Chattah et al., 2009; Miura et al., 1998; Nikolai, 1996; Smith and Burstone, 1984). With the combination of translation and rotation it is crucial to have sufficient movement space within the alveolar socket to avoid hard tissue contact and resulting stress peaks. Nikolaus et al. (2017) found in chewing events simulated by finite element modelling in three-rooted teeth that small spatially-varying geometric adjustment to the thickness of the PDL lead to strong changes in tooth reaction movements, as well as PDL and bone stress (Nikolaus et al., 2017). Moreover, it has been reported that pig, mini-pig and rat lower and upper molars under load rock or tilt with an additional pushing movement into the alveolar socket (Chattah et al., 2009; Naveh et al., 2012b; Salamati et al., 2020). Based on digital image correlation (Lin et al., 2013) suggested the combination of translation and rotation results in a "screw-like-motion", thus promoting both compression and tension at specific locations within the tooth-PDL-bone complex. In terms of bone remodeling processes it has been argued that compressive strains are related to resorption in alveolar bone, while tensile strains promote mineral formation (Jang et al., 2018).

Microscopic measurement studies in pigs (Salamati et al., 2020), bovines (Bosshardt et al., 2008; Pini et al., 2004; Sanctuary, 2003), rats (Chiba et al., 1990; Preissecker, 1931; Zanoni et al., 2013) and humans (Coolidge, 1937; Jozat, 1933; Klein, 1928; Schroeder, 1986) have shown that the thickness of the PDL space differs between species and by tooth position. Additionally variations in the loading regime, i.e. the loss of the antagonistic tooth and resulting lower antagonistic forces results in a widening of the periodontal space (Coolidge, 1937; Jozat, 1933; Klein, 1928). For example, in human incisors and premolars the PDL thickness ranges from 170 up to 390 μm (Klein, 1928), while it is 221–785 μm thick in first molar in bovines and 165 μm – 206 μm thick in incisors of rats. The PDL space for all human teeth shows a non-uniform thickness distribution along the long axis of the tooth root, i.e. the PDL is thicker in both the cervical and apical region compared to the mid-root region (Klein, 1928; Schroeder, 1986). This configuration is known as a double cone goblet shape and allows the tooth to tilt within the alveolar bone.

Besides the shape of the PDL, the vascular system is also considered to guide tooth movement. The blood vessels allow for pressure compensation through fluid displacement which, in turn, affects the biomechanical response to loads applied to the tooth (Bien, 1966; Radlanski, 2011). Additionally, the systemic blood pressure in the vessels of the PDL results in a measurable pulsation of a tooth under loading (Imamura et al., 2002; Ng et al., 1981). Vessel distribution is affected by the applied loading regime. The absence of the loading regime results in a decrease of the vessel concentration, whereas the application of orthodontic forces leads to an increase (Murrell et al., 1996). Moreover, a study of bovine PDL suggested that higher functional loads herbivores compared to human results in a higher concentration of blood vessels in the apical region of the PDL compared to other regions along the tooth root axis (Bosshardt et al., 2008).

The aim of the present study is to link the shape of the PDL space and the vascular distribution to the 3D loading behaviour of the tooth in the grey mouse lemur (*Microcebus murinus*). Specifically, this study investigates whether a screw-like motion, as observed in the multi-rooted teeth of rats and mini-pigs, also occurs in non-human primates. The molars of *Microcebus* are of the tribosphenic type, which is found in several placental orders including basal primates such as the strepsirrhines (e.g. Swindler, 2002). They are bucco-lingually wide with more pointed and crested molar cusps owing to their fruit, gum and insect eating feeding behaviour (Chazeau et al., 2013; Dammhahn and Kappeler, 2008; Zablocki Thomas et al., 2018).

Following previous experimental tooth loading studies (Lin et al., 2013; Naveh et al., 2013; 2012b;; Pal et al., 2017) we used a non-destructive high resolution imaging approach and combined it with a loading setup. Micro-computed tomography with synchrotron radiation techniques (SRμCT) allow for the visualization of internal tooth morphology and even resolves tooth ultrastructure (Dalstra et al., 2015; Le Cabec et al., 2019; Tafforeau et al., 2012). We employed SRμCT in combination with an *in situ* loading device to perform *in vitro* a quantitative displacement and structural analysis on molar teeth of *M. murinus*. The advantage of using SRμCT over "conventional" laboratory based CT-systems is the use of high flux, the availability of additional contrast modalities e.g. single-grating and single distance based phase-contrast micro tomography enabling the simultaneous detection of soft and hard tissue structures at highest spatial resolution and the fast scanning time, which is important for *in-vitro* experiments with biological tissues.

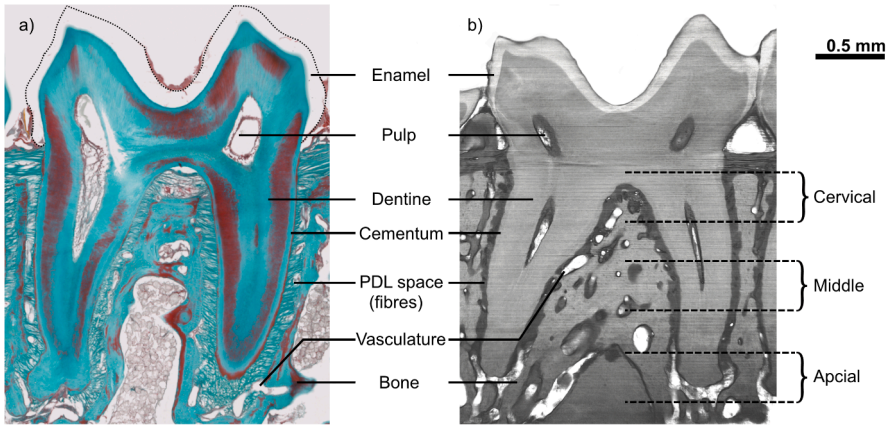

Fig. 1. a) Trichrome stained microscopic slice of an upper second molar (M2, lateral view, specimen ML03), black dots represent the border of the enamel (note that the enamel was dissolved during the decalcification process of the staining procedure; b) Virtual slice of a synchrotron scan (DESY) of an upper second molar (M2, lateral view, specimen ML01.1). EDJ = Enamel – dentine – junction; CDJ = Cementum – Dentine – junction.

2. Material and methods

2.1. Samples and specimen preparation

Eight adult female cadavers of grey mouse lemurs (*Microcebus murinus*) ranging in age from 2 to 7 years were obtained frozen from two captive mouse lemur colonies in Paris (UMR7179, Muséum National d'Histoire Naturelle, Brunoy, France) and Hannover (Institut für Zoologie, Tierärztliche Hochschule Hannover, Germany) (Table 1). The specimens were stored frozen at −20 °C. At the time of the scanning experiments, the samples were defrosted at room temperature. We then dissected both the upper and lower jaws and removed the soft tissue around them (Fig. 2A, Supplementary Figure 1A). Each jaw was cut into blocks of 3.5 × 3.5 × 2 mm^3 using a micro grinder (Emax Evolution, NAKANISHI Inc., Shimohinata, Japan). The blocks contained the upper and lower second molar (M2), respectively, flanked by half of the neighbouring teeth (first and third molars) (Fig. 2B, Supplementary Figure 1B). Following preparation, the samples were stored in physiological Ringer's (147 mmol/l Na^+, 4 mmol/l K^+, 2.3 mmol/l Ca^{2+}, 156 mmol/l Cl^-) solution to prevent drying.

2.2. Loading and imaging experiments

The scanning and loading experiments were conducted at two synchrotron facilities. Six experiments were performed in our study on the ID19 imaging beamline of the European Synchrotron Radiation Facility (ESRF, Grenoble, France) (Erko et al., 2015). In addition, two experiments were performed at on the imaging beamline P05 at the German Electron Synchrotron in Hamburg (DESY, Germany) which is operated by the Helmholtz-Zentrum Geesthacht at the PETRA III storage ring (Haibel et al., 2010b; 2010a). Both synchrotron imaging facilities allowed us to use phase contrast to image both soft and hard tissues at the same time and offered custom-made axial loading devices used for X-ray micro-tomography experiments (see detailed description below). The SYNCHROLOAD loading device at DESY is vertically aligned and is mounted onto the standard air bearing rotation axis of the tomography setup (Supplementary Figure 2A,B) (Willumeit-Römer et al., 2018). The TomoPress of the ESRF is a horizontal setup (Supplementary Figure 2C, D) and holds two synchronized rotation stages to turn the sample in the x-ray beam (Rack et al., 2020). Both setups were equipped with an actuator (loading pin) and a load cell (Supplementary Figure 2B,C,D). Each alveolar bone sample containing the M2 was glued onto a sample holder (Supplementary Figure 2D) using a resin (Z100 MP restorative paste, 3 M ESPE Dental Products, St. Paul, U.S.) and hardened by ultraviolet light source (HS-LED light 200, Henry Schein Inc., Melville, U. S.). In addition, a thin layer of the resin was placed on the crown occlusal surface to create a flat contact area with the loading pin to avoid shear forces caused by the irregular surface of the crown (Fig. 2B, 3A,B, Supplementary Figure 1B, 2B,D) to avoid shear forces. This was done by carefully moving the loading pin in the z-direction without contacting the crown surface before hardening the resin with an UV light source (see above). To not restrict any movement direction during loading the loading pin and the resin had just surface contact and no fixed connection. Additionally, the long axis of each of the tooth crown were placed vertical to the loading pin. This was also controlled by the CT projections during loading preparation. In order to avoid any movements related to drying of the samples a humidified atmosphere was created by placing water-soaked tissue papers beneath the samples. While the SYNCHROLOAD setup provides a closed volume by design, the TomoPress has an open chamber, which was sealed with Kapton foil during the experiment to maintain constant humidity (Supplementary Figure 2C,D). Additionally, at the ESRF we moisten the samples with an integrated pumping mechanism. Each specimen was then scanned without any load application (unloaded scans, Fig. 3A) with the following imaging modalities:

1) At ESRF the tomograms were acquired with a (pink) photon energy of 34 keV, using an undulator (u17.6) with a gap of 13.5 mm and filters of aluminium (2.8 mm), copper (0.14 mm) and diamond (1 mm).

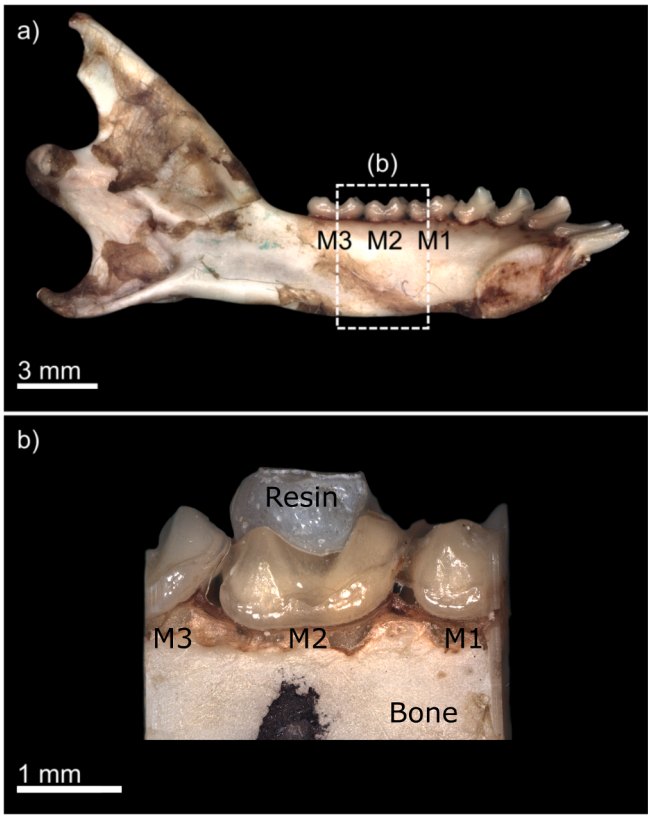

Fig. 2. a) Left mandible of ML04 with the sampling region ((b), white dashed line); b) Sample for loading experiment including the target tooth (M2) and half of the neighbouring teeth (M1 and M3, respectively). The acrylic resin on top the crown was used as a buffer between the crown and the loading pin (not shown; see Fig. 3 and text for details).

Table 1
Mouse lemurs (with accession numbers) used in study, loads applied to teeth and scan resolution.

Exp.no	Beamline	ID	Bone	Site	Sex	Age [years]	Load [N]	Voxel size [μm]
ML01	ESRF	223 GB	mandible	right	female	3	18.6	1.85
ML01.1	ESRF	223 GB	maxilla	right	female	3	18.6	1.85
ML02	ESRF	252AB	mandible	right	female	5	18.1	1.85
ML03	ESRF	263BCC	mandible	right	female	2	18.3	1.85
ML04	ESRF	288BB	mandible	right	female	2	17.8	1.85
ML05	ESRF	245BA	maxilla	left	female	4	18.1	1.85
ML06	DESY	Peggy	maxilla	right	female	4	4.4	2.57
ML07	DESY	Saphira	maxilla	left	female	7	4.5	2.57

(Exp.no = experimental number specimen ID at the MPI, ID = original specimen ID from the respective lemur colonies). DESY = German Electron and Synchrotron Centre, ESRF = European Synchrotron and Radiation Facility.

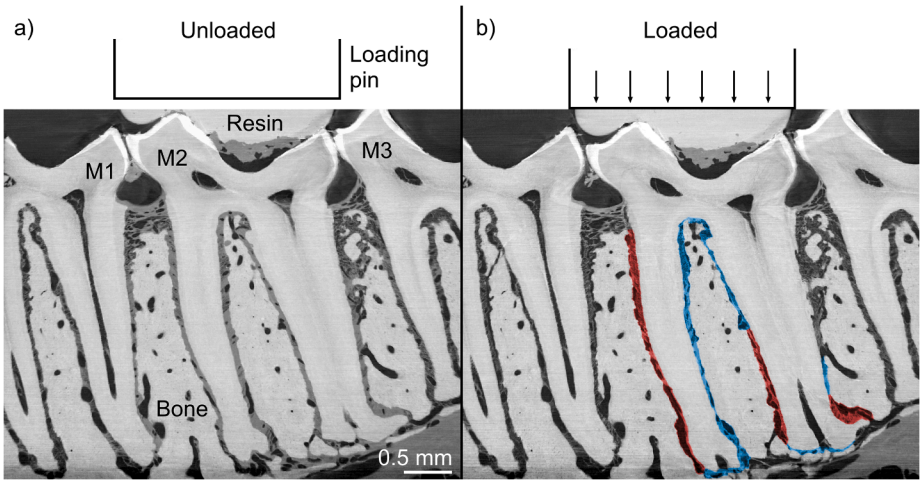

Fig. 3. Micro-CT sections of the of the mandibular molars of *Microcebus murinus* showing the target tooth (M2) and neighbouring teeth (M1 and M3) a) without load, and b) under compressive axial load. The regions of the PDL space under compression are coloured in blue, while regions under tension are shown in red. Note the newly formed gap between the M2 and M3 crowns and the displacement of the M2 into the alveolar socket when compressed. The schematic above the teeth illustrates the position of the loading pin and load direction.

The effective pixel size in the reconstructed images was 1.85 μm (FReLoN CCD camera type e2v, lens-coupled with 8x magnification (4x front lens with 0.16, 2x eye-piece) to a 100 μm thin LuAG:Ce scintillator). Due to the above photon energy and the relatively coarse pixel size a drift space of 1.15 m was left between sample and detector in order to benefit from phase-enhanced contrast. Single-distance phase retrieval technique was applied in order to increase the contrast and to switch from edge-enhanced regime to area contrast for subsequent image analysis. 1000 projection images were recorded per tomographic scan over 180 degrees with an exposure time of 0.2 s.

2) At DESY, tomographic imaging was conducted at a photon energy of 35 keV using a single-grating Talbot interferometer technique using a phase-grating with period p1 = 10 μm and a structure height of 10.4 μm, inducing a phase-shift of π/2 at its design energy of 60 keV (Hipp, 2019; Hipp et al., 2016). For this beam setup using a monochromator no filters were needed. By tilting the grating towards beam direction, the effective structure height was adjusted appropriately to the selected photon energy. For the measurement a custom build CMOS-based camera system with an effective pixel size of 1.3 μm and a dynamic range of 12 bit was used (Lautner et al., 2017). For each tomogram a series of 1201 projections were taken with a sample rotation over 180 degrees. For each projection a series of four images (three phase steps) was recorded.

Following the scanning without load application each specimen was then scanned with an axial load of up to 19 N at ESRF (TomoPress) and - due to technical limitations of the SYNCHROLOAD setup - with 5 N at DESY (Willumeit-Römer et al., 2018) (loaded scans; Table 1, Supplementary Figure 2B). Both loads were well within published maximum bite force values of 36 N for female mouse lemurs which are known to bite harder than males (Thomas et al., 2015). Due to the limitation of the experimental setup, we assumed that no flexural deformation occurs at the bony tissue. The applied forces were relatively small and the load was applied perpendicular onto the crown, which reduced shear forces. Additionally, the complete bottom of the small sample block were attached perpendicular to the applied force direction, what reduces any lever arm mechanics, which can result in flexural deformation. Before scanning under load, each specimen had a relaxation time of 5 min. This was deemed necessary to minimize the influence of transient processes in the material (especially the fluid phase of the PDL) and to improve image quality. The scanning time for each setup was about 30 min for the different scenarios. It is important to note that based on the inspection of the scans we did not observe any damage of the PDL due to freezing or thawing of the specimens.

2.3. Image processing and registration

In the software Avizo version 9.3 (Thermo Fisher Scientific, Inc.) we converted the original tomographically reconstructed 32-bit floating point image stacks into 16-bit gray scale images to reduce computational time and space usage. In the same software we then performed a landmarked-based registration with an affine transformation algorithm to register the loaded and unloaded datasets. Landmarks were set manually at the alveolar bone in the scanned images under the assumption that the bone did not perform any or just minimal displacements during loading. Landmarks were set on unambiguous areas that could be identified at the unloaded and loaded CT images e.g. vessel branches in the bone. The registrations process was done three times in a row to have a higher reliability. After the registration process, randomly chosen slices were compared to identify the equivalent structures and the loaded and unloaded corresponding CT images.

To estimate the displacement between the unloaded and the loaded teeth a second landmark-based registration was performed to estimate displacements for the unloaded-loaded configuration. All registration steps were done on the voxel data to avoid segmentation errors. After completing the registration the unloaded M2s were segmented with the Biomedical Image Segmentation App (Biomedisa) (Lösel and Heuveline, 2016). For both tooth models, the same point cloud was used for triangulation and fitting. In other words, we first created a surface model of the unloaded tooth, with a number of 500,000 points for the triangulation. Next, we created the model of the loaded tooth by using a search algorithm of surface point fitting (in Avizo, 9.3). The sum of triangles per surface model was set constant.

For alignment of the directions, the teeth were transformed by their centre of gravity into the origin of the X, Y, Z-coordinate system, where the X-axis represents the buccal-lingual direction, the Y-axis as the mesial-distal direction and the Z-axis the coronal-apical direction. We assumed that the tooth acted like a rigid body and the displacement was guided by the PDL as the softest component in the tooth-bone complex.

2.4. Computation of displacements

Differences in all spatial (X, Y, Z) directions were computed to quantify tooth displacement in MATLAB R2016b (incl. Image Processing Toolbox, The MathWorks Inc.). With the corresponding points of the loaded and unloaded surface models, it was possible to estimate the absolute orientation of the teeth using the method of Horn (Horn, 1987). We computed the fitting between the two surface models (loaded and unloaded) in MATLAB using an algorithm, which minimizes the distance between the two models. The fitting results of the surface models were limited to the numerical estimation of MATLAB and the computed movements may be lower than the effective pixel size of our image data. For the displacement evaluation we assumed a rigid body movement implying that the tooth movement is guided by the PDL as the softest

component between bone and tooth (Ho et al., 2007). In addition, because of the large-scale differences in the stiffness of the hard and soft tissues involved and the relatively small loads applied we assumed that the bone and dental tissues (enamel, dentine and cementum) only deformed minimally during the loading procedure.

We estimated displacements for all three translational and rotational directions. For evaluating the values we used an orthogonal coordinate system, where the X-axis represents the displacements in the buccal (+) and lingual (-) direction; the Y-axis represents the mesial (+) and distal (-) direction; and the Z-axis represents the coronal (+) and apical (-) direction (Supplementary Figure 3A, B). The absolute 3D displacements were measured as ×, y, z translations in micrometres [µm] and the rotations around the three axes in Euler-angles [°] in the following sequence Z-Y-X. From these the Euclidean distance between the corresponding points of the vertices between the unloaded und loaded tooth models were computed to visualise the displacement pattern for each molar. The colour map was standardized for each specimen to compare regions with high and low displacements among all teeth.

2.5. Analysis of PDL space morphology and vascularization

The unloaded image stacks of the two-rooted mandibular M2s and three-rooted maxillary M2s were each split into three volumes of interest (VOIs) of 200 – 300 µm in height along the tooth root axis (Fig. 1B, 7, 8). The cervical VOI included the PDL beneath the alveolar bone crest and the root furcation; the middle VOI included the mid-root section; and the apical ROI covered the apical portion of the root. Within these ROIs we manually segmented the PDL space in Avizo and used a thickness algorithm implemented in Avizo (Hildebrand and Rüegsegger, 1997) applied to each resulting label field to compute the PDL thickness (in µm). The algorithm fitted maximal spheres to every point inside the structure and assigned local thickness values (Hildebrand and Rüegsegger, 1997).

To analyse the vascularization in the PDL space, we filtered the three VOIs with a non-local-means filter (Buades et al., 2005) in Avizo with a kernel size of 5x5x5 voxels in Avizo to enhance the contrast and avoid segmentation of non-relevant structures smaller than 3 voxels within the PDL. Following (Bosshardt et al., 2008) we assumed that the circular non-filled structures within the PDL gap represent the vasculature. The user segmented the vessels with a semi-automatic algorithm (a grey-value based 3D region growing) including a manual correction. The remaining voxels were defined as other PDL tissue. To compute the volume ratio (in %) between vessels and other tissues the material statistics tool in Avizo was used. Directionality analysis of the PDL was performed with a self-written MATLAB code, including a manual correction for the tooth root curvature. Each ROI was split into 24 different sections every 15 degrees and a mean value for the PDL thickness and vessel volume ratio for every section was computed. In total we obtained 14 datasets representing VOIs. Mandibular M2s were split into mesial and distal roots (6 VOIs), whereas maxillary M2s were split into a bucco-mesial, a bucco-distal and lingual root (8 VOIs). Since the lingual root was considerably shorter than the buccal roots (see Supplementary Figure 2A), this root was divided into two VOIs (only cervical and middle) whereas the middle portion of the lingual root represents its apical region.

3. Results

3.1. Tooth root morphology

All *Microcebus murinus* specimens had two and three roots in their mandibular and maxillary molars, respectively (Fig. 5). The tooth root tips in both, mandibular and maxillary molars were bulb-shaped (Figs. 4 and 5). While the tooth crown long axis was almost perpendicular to the occlusal plane, the root axis deviated from that of the crown in the distal direction (Fig. 4).

3.2. Tooth displacement

Six out of the eight M2s (mandibular and maxillary) were loaded with a maximum force of 18.6 N, while two maxillary M2s specimens (ML06 and ML07) were loaded with 4.5 N (Table 1) resulting in relatively lower absolute displacements (z-direction) in the latter (Table 2). In four out of eight samples, the resin partially covered the neighboring tooth crown but not the bone (Table 2, Supplementary Figure 4). We also observed contact between the resin and the mesial part of the neighbouring tooth crown. However, we did not find a consistent pattern that was reflected in the loading results. Moreover, no additional translations besides the z-axis direction were found and we refrain from linking an earlier tooth bone contact to such reason. The inspection of

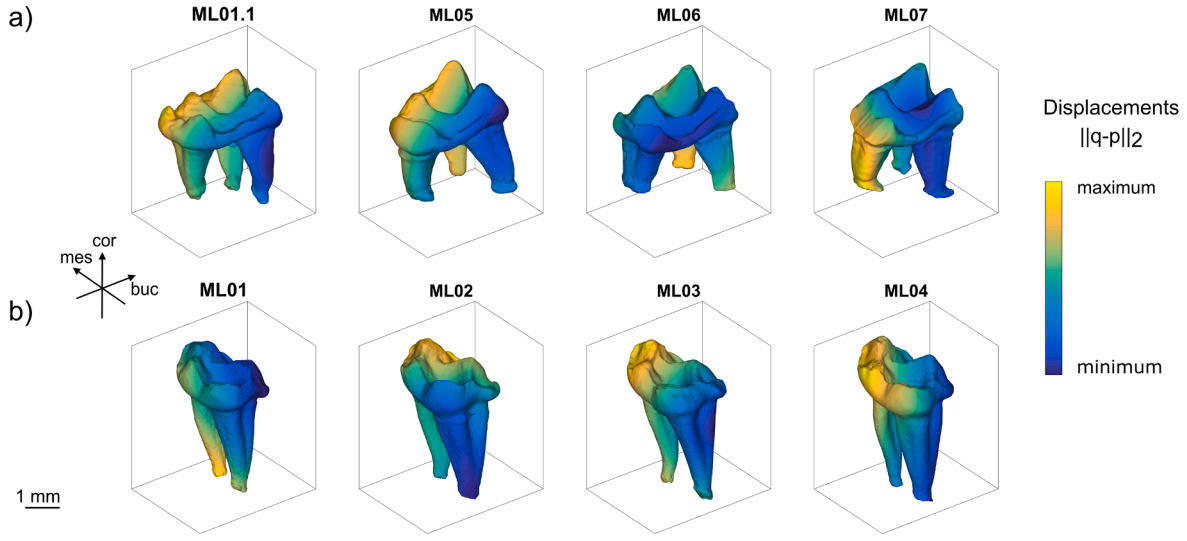

Fig. 4. Euclidean distance ($||q-p||_2$) maps of the displacements between the corresponding unloaded and loaded teeth in a) maxillary and a) mandibular M2s. Note that for comparative purposes the displacements of each molar were transformed to provide a qualitative representation of the maximum and the minimum displacements only (without units). The real displacement values are shown in Table 2. Note also the broadened root tips of the roots in both mandibular and maxillary M2s.

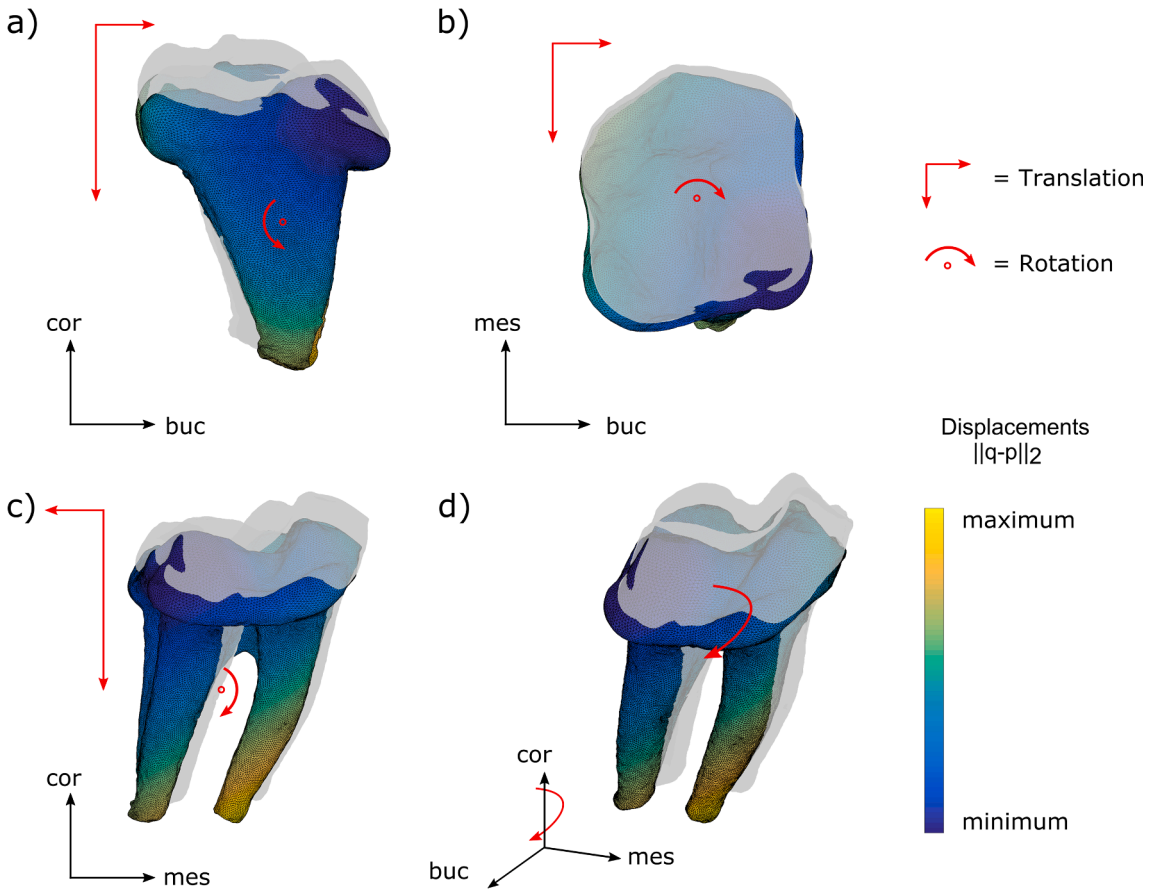

Fig. 5. Translation (red arrows) and rotation (red curved arrows with the rotation centre) of a mandibular M2 under load (specimen ML01) compared to the unloaded condition (white silhouette. a) distal view; b) occlusal view; c) buccal view; d) mesio-buccal view.

Table 2
Absolute 3D displacements (translation and rotation) of mouse lemur molars under axial load (in z direction).

		Translation			Rotation		
Bone	Specimen	X [µm]	Y [µm]	Z [µm]	Rot X [°]	Rot Y [°]	Rot Z [°]
Maxilla	**Ml01.1** *,#	−2.80	−1.70	−33.32	−0.83	−0.28	−0.10
	ML05 #	8.76	1.42	−19.10	−0.47	−0.09	−0.36
	ML06 *	2.85	−3.87	−5.06	−0.21	−0.01	−0.19
	ML07	3.18	2.35	−5.48	0.04	−0.05	−0.48
Mandible	**ML01**	3.81	−4.92	−8.48	−0.10	−0.26	−0.17
	ML02 #	−2.43	4.51	−13.80	−0.20	0.07	0.17
	ML03 #	−5.38	−3.79	−17.01	−0.61	−0.53	0.26
	ML04	−3.71	5.10	−31.18	−0.10	−0.09	−0.22

* Model mirrored virtually to align with other models.
# Resin partially covered the neighbouring tooth crown.

the loaded CT scans revealed only one specimen (ML01.1) with contact between the tooth roots and the alveolar boneat the furcation area (Supplementary Figure 4).

Both mandibular and maxillary M2s experienced the highest translational displacements in the apical (-Z) direction, whereas the displacements in the bucco-lingual (X) and mesio-distal (Y) directions were consistently lower and more variable in magnitude (Table 2; Fig. 5). The combination of rotation and translation in mandible for specimen ML01 are shown in Fig. 5. The displacement in the maxilla for specimen ML01.1 it is shown in Fig. 7. The rotation around the different axes resulted in different displacement magnitudes for the tooth in different regions (Fig. 5 A,B,C,D- and 6 A,B,C,D). Considering the dimensions and rotation centre of the average mouse lemur molar (see Supplementary Figure 3) we computed that the rotation of 0.1 degree around the bucco-lingual (x) axes results in a movement of around 3 µm for areas with the maximum distance to the rotations centre (e.g. tooth root tips). Rotation resulted in the highest movement crown region and the root-tips (Figs. 5 and 6). In turn, a 0.5 degree rotation corresponded to a 15 µm movement (see Table 2).

All maxillary M2s rotated clockwise (-Z) around the long axis of the tooth. Two mandibular M2 (ML01 and ML04) rotated clockwise (-Z), while the other two (ML02 and ML03) rotated counter clockwise (+Z). The rotations around the bucco-lingual (x) axis and the mesio-distal (Y) axis were negative in both mandibular and maxillary M2, i.e. the crowns tilted both mesially and lingually, while concomitantly the roots tilted distally and buccally (Table 2; Fig. 4). In all maxillary M2s, the highest displacements occurred in the mesial half of the crown and the mesio-buccal root except for ML07 where the lingual portion is subjected to the highest displacements (Fig. 4A). In three out of four maxillary M2s the displacements were lowest in the bucco-distal portion of the crown

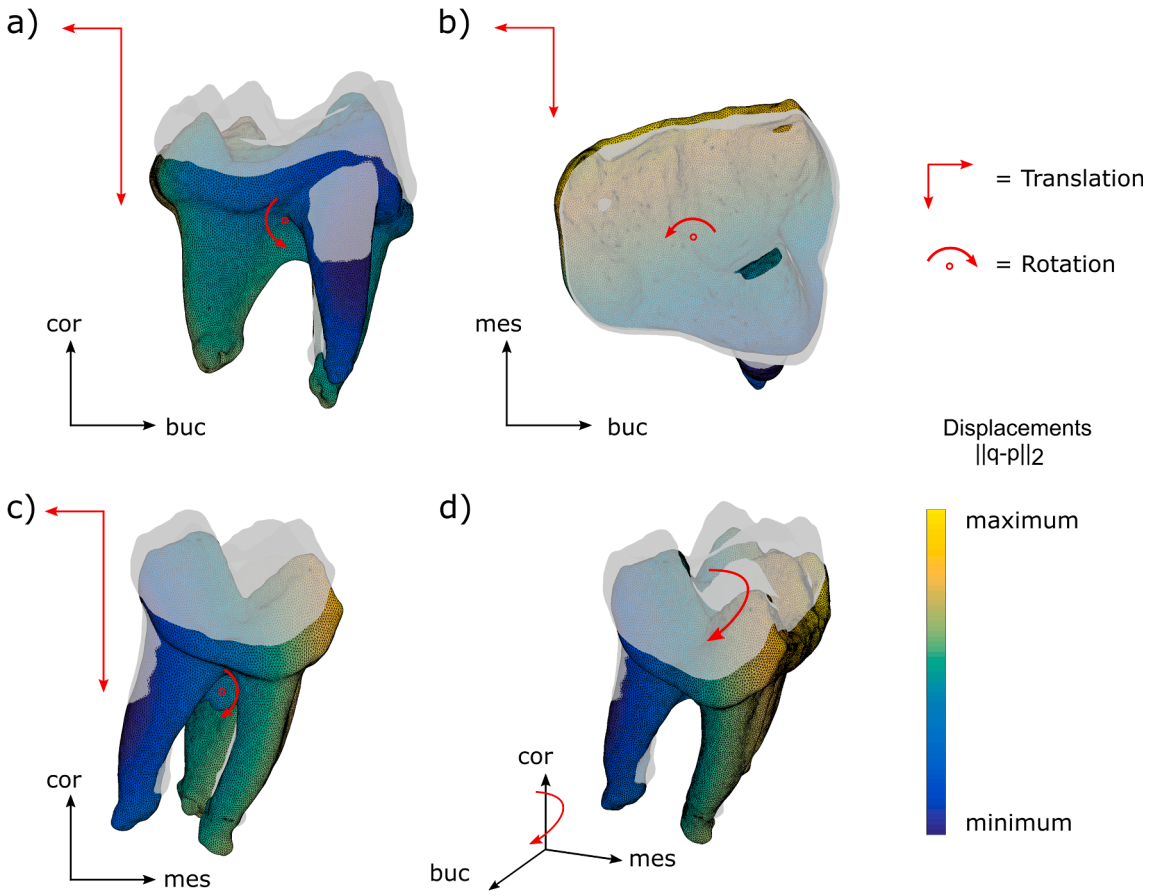

Fig. 6. Translation (red arrows) and rotation (red curved arrows with the rotation centre) of a maxillary M2 under load (specimen ML01.1) compared to the unloaded condition (white silhouette). a) distal view; b) occlusal view; c) buccal view; d) mesio-buccal view.

and root, except for ML06 where the linguo-distal part of the tooth moved the least. In the mandibular M2s, displacements were largest in the mesial half of the tooth (crown and mesial root), while the lowest displacements were generally found in the distal half of the tooth (Fig. 5B).

3.3. PDL space morphology

The mean PDL space in the unloaded teeth was generally wider in the mandibular M2s than in the maxillary M2s (Table 3; Fig. 7). In general, the PDL spaces of both mandibular and maxillary M2 roots were hour-glass shaped, i.e. both the apical and cervical regions were wider than the mid-root (Table 3; Fig. 7). In the mandibular M2s the thickness was similar in both mesial and distal roots, i.e. the apical > cervical > mid-root region (Table 3; Fig. 7). In the maxillary M2s, all three roots showed the following PDL thickness distribution: apical > cervical = mid-root (Table 3; Fig. 7). In both mandibular and maxillary M2s the width in each section was relatively similar, with the exception of the cervical region (disto-lingually expanded) of the lingual root in the maxillary M2 and the cervical region of the mesial (mesio-buccally expanded) and distal roots (disto-buccally expanded) of the mandibular M2 (Table 3; Fig. 7). It is noteworthy that the palatal roots of the maxillary teeth were significantly shorter compared to the buccal roots (Fig. 7).

Loading the teeth resulted in a compression of the PDL space of up to 14% in nearly all regions along the tooth root axis, except for the bucco-distal root in the cervical region of the maxilla, where a widening of the PDL space occurred (Table 3, Fig. 4B).

3.4. PDL vascularization

In both maxillary and mandibular M2s the PDL space was highly vascularized and the vasculature surrounded the complete root like a net-like structure (Fig. 8). In both mandibular and maxillary M2s there was a gradual increase in the volumetric proportion of the vessels from cervical to apical (Table 3). The apical region of the maxillary M2 roots was more vascularised than that of the mandibular M2s (Table 3; Fig. 8). Moreover, the volume ratios in both mandibular and maxillary M2s were not uniformly distributed around the circumferences of the root subsections. In particular, the vessels in the cervical region of all three maxillary M2 roots were more concentrated in the furcation area of the tooth, while in two buccal roots the volume ratio was highest on the lingual aspect in the apical region (Table 3, Fig. 8). In the mandibular M2s, the volume ratio in the cervical region was highest on the distal aspect of the mesial root and on the mesial aspect of the distal root (Table 3, Fig. 8).

4. Discussion

This study is the first of its kind to investigate the form-function relationships between the tooth movement during load and the PDL shape and vascular distribution within the PDL space in a non-human primate species. *Microcebus murinus* has the same tooth root morphology as other primates including humans, i.e. mandibular and maxillary with two and three roots, respectively. Moreover, the molar root axis deviates from that of the crown long axis which is not unusual for primates and also found in humans (see e.g. Kupczik and Dean, 2008). This particular root deflection found in primates is different to that of other mammals such as rats, mice, and mini-pigs where the tooth

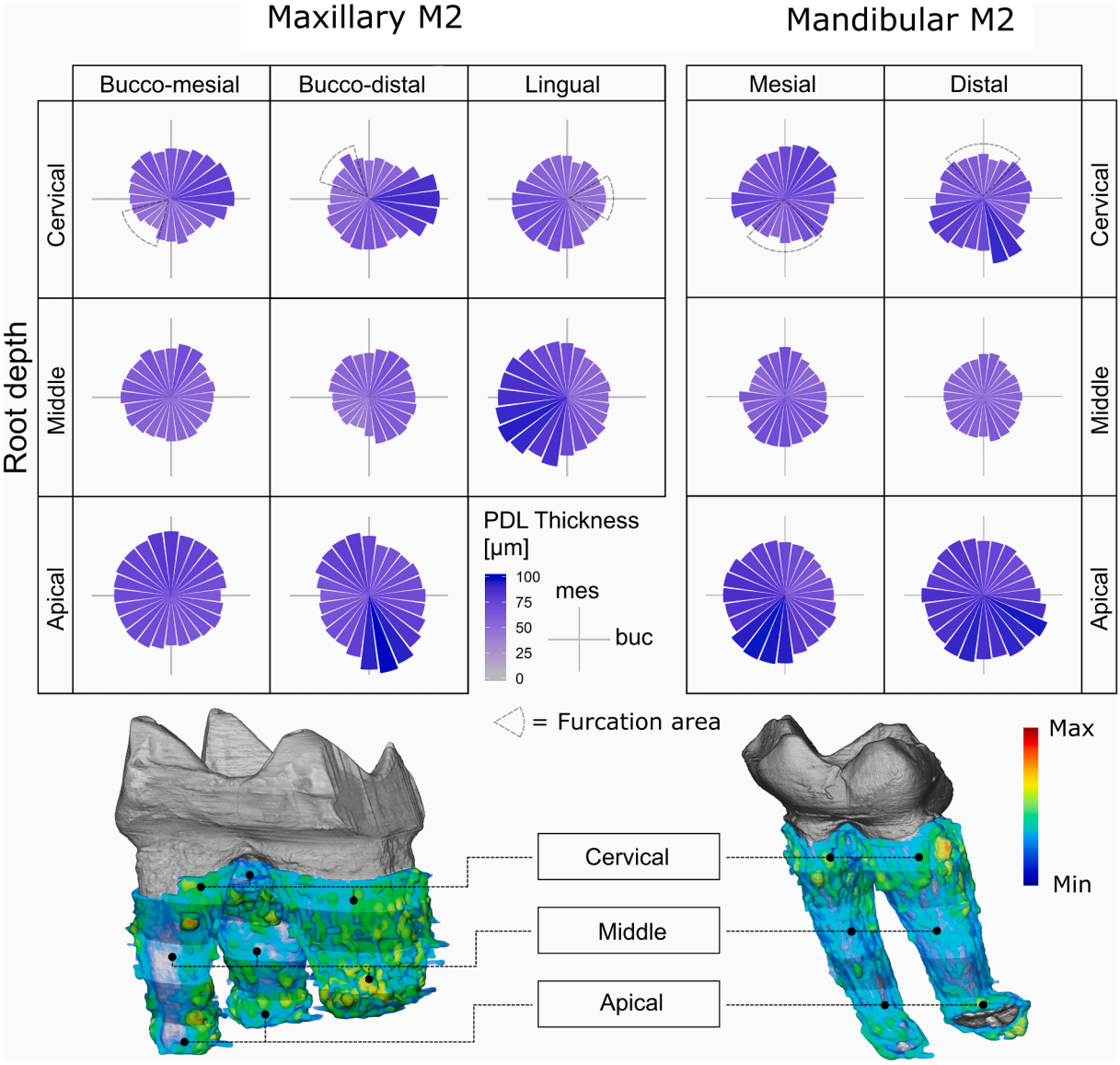

Fig. 7. Star diagrams of PDL thickness in the 3-rooted maxillary and 2-rooted mandibular M2s, respectively, at three depth levels along the root long axes (as indicated in the illustration below). In addition, the colour-coded maps projected on the roots illustrate the variations in PDL thickness.

Table 3
Mean values and standard deviation of the PDL space width for the unloaded and loaded teeth and the vasculature [volume %]. The maxillary and mandibular roots were divided in distinct regions (volumes of interest) along the tooth roots.

Bone	Region	Root	PDL space unloaded [µm]	PDL space loaded [µm]	Difference [%]	Vasculature [%]
Maxilla	Cervical	Bucco - distal	69.69 ± 26.34	70.23 ± 28.98	+0.77	12.17
		Bucco - mesial	63.90 ± 24.05	61.80 ± 24.96	−3.40	13.11
		Palatal	64.21 ± 23.55	62.57 ± 25.90	−2.62	9.80
	Middle	Bucco - distal	62.70 ± 20.01	59.22 ± 21.06	−5.87	16.90
		Bucco - mesial	66.09 ± 20.78	65.08 ± 22.85	−1.55	13.71
		Palatal	82.88 ± 31.40	77.89 ± 32.25	−6.41	14.78
	Apical*	Bucco - distal	85.53 ± 35.48	75.06 ± 28.03	−13.95	21.90
		Bucco - mesial	80.49 ± 26.40	76.79 ± 28.88	−4.82	20.45
Mandible	Cervical	Distal	72.80 ± 23.05	68.57 ± 23.89	−6.17	14.13
		Mesial	70.52 ± 22.42	64.41 ± 21.73	−9.49	11.81
	Middle	Distal	58.22 ± 18.94	53.97 ± 18.97	−7.87	17.59
		Mesial	64.55 ± 20.60	61.34 ± 22.16	−5.23	14.24
	Apical	Distal	88.37 ± 33.06	82.67 ± 32.03	−6.89	21.83
		Mesial	85.98 ± 31.99	82.41 ± 32.31	−4.33	21.92

* Due to the fact that the palatal root is relatively shorter than the two buccal roots, no apical region was defined.

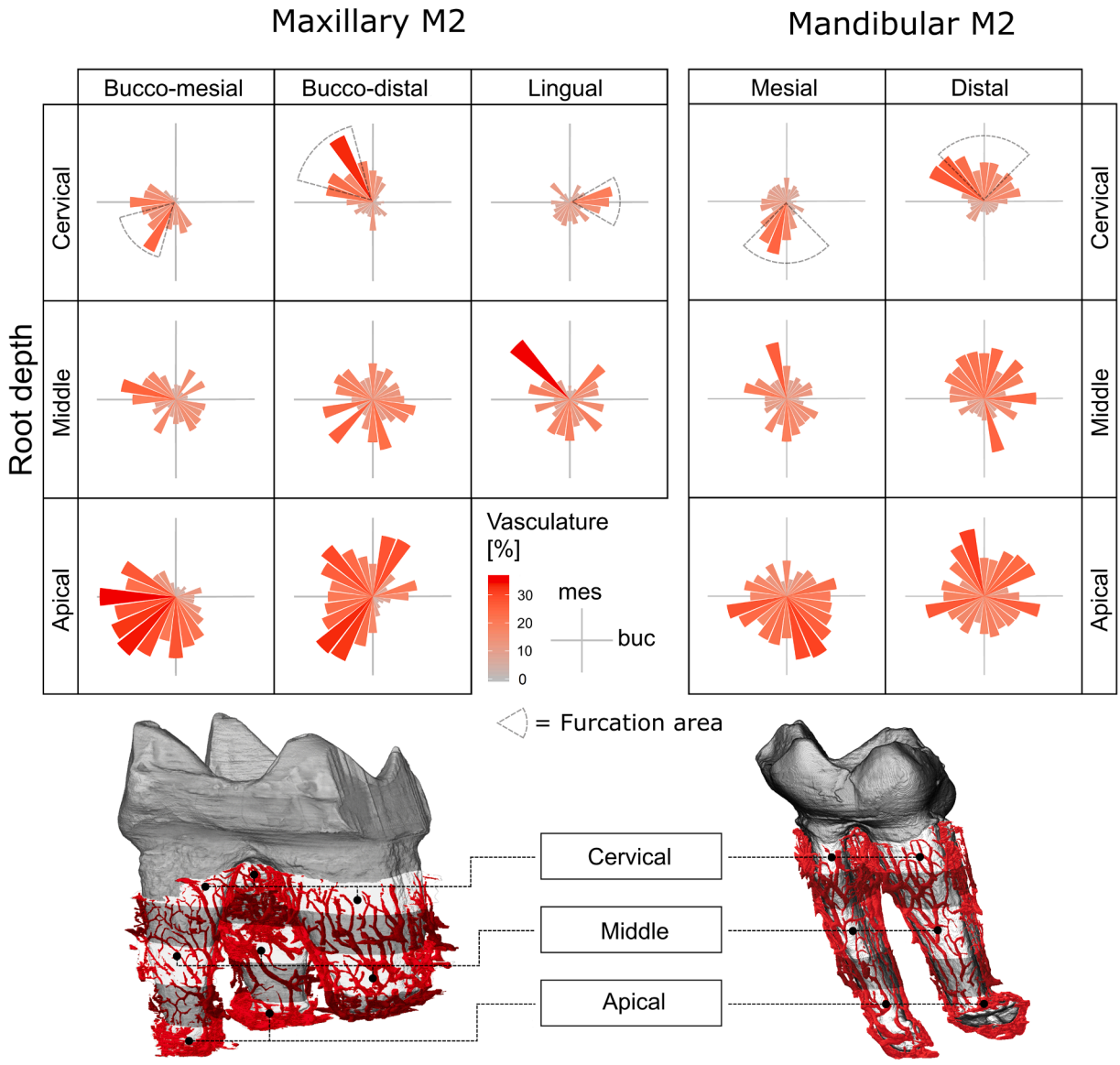

Fig. 8. Star diagrams showing the PDL vasculature density in the 3-rooted maxillary and 2-rooted mandibular M2s, respectively, at three depth levels along the root long axes (as indicated in the illustration below). The vascular network is also illustrated in the 3D reconstructions below.

long axis forms a straight line (see for example Naveh et al. 2012, Ben-Zvi et al. 2019).

4.1. PDL space morphology

The measured values of mouse lemur PDL width (thickness) show a high standard deviation. These large thickness variations can be explained by the curvature of the PDL especially at the bony site which is also reported in bovine teeth (Bosshardt et al., 2008). In all regions of PDL the vessels can be found which occupy the complete PDL gap and create typical curvature of the bone around the PDL (Fig. 9). We assume that the narrowing of the PDL (Table 3) mainly occurs that the tooth is moving into the bony socket.

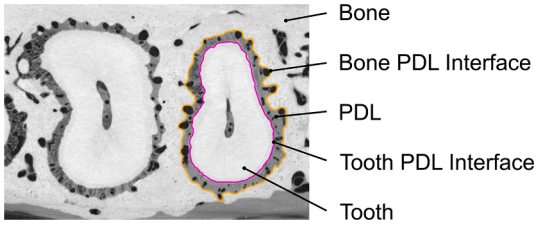

Fig. 9. Micro-CT section of a mandibular molar root showing the tooth-PDL interface (magenta) and the irregular shape of the bone-PDL interface (orange).

Our results indicate that the PDL space of the mandibular molars of *M. murinus* has a double goblet or hour-glass shape, and is thus similar to that of humans (Klein, 1928; Schroeder, 1986) and rats (Chiba et al., 1990; Preissecker, 1931; Zanoni et al., 2013). Based on the shape of the PDL space we suggest that the shape is optimized for a rotation around the narrowest section of the PDL, which is located in the middle, halfway along the long axis of the tooth root (Fig. 1). In contrast, the PDL space of the maxillary molars is widest around the apex (PDL thickness: apical > cervical = mid-root); a finding shared with pig molars (Salamati et al., 2020). It is therefore likely that in maxillary molars the rotation point is located more towards the tooth cervix. Especially during large rotational movements the areas with a higher radial distance to the narrower sections require more space during their rotational movements to avoid contact between the bony socket and the tooth (Salamati et al., 2020; Smith and Burstone, 1984; Yoshida et al., 2001). This is particularly the case for the cervical and apical regions of the mandibular molars. We

therefore suggest that, at least in the mouse lemur sample of our study, the PDL shape is optimized for more rotational movements around the narrower sections of the PDL space (see also discussion on tooth movement below).

4.2. PDL vascularization

We found a high concentration of vessels in pressure dominated areas, in particular at the tooth root tips and in the root furcation area (Fig. 8). In general, the distribution of the vessels within the molar PDL space, which is supplied by the inferior alveolar artery and the posterior superior alveolar artery, respectively, shows a marked gradient along the longitudinal axis of the teeth. Thus, and similar to what has been reported for humans (Radlanski, 2011), rats (Jang et al., 2015; Kindlov and Matena, 1962) and bovines (Bosshardt et al., 2008), the least amount of vessels was found in the cervical region, while the majority of vessels were located in the apical region (Fig. 8). Our results therefore provide further support that the periodontal vascularization contributes to a hydrodynamic dampening mechanism. It implies that under physiological conditions a systemic blood pressure and fluid displacement towards the ground matrix form an integral part of the damping mechanism, which has been suggested, to help compensate pressure peaks and avoid tooth bone contact or damage (S. M. Bien, 1966b; Saul M. Bien, 1966a; Picton, 1990).

4.3. Tooth movement

Using a similar experimental setup to earlier studies (Chattah et al., 2011; 2009;; Lin et al., 2013; Naveh et al., 2012a) we subjected the mandibular and maxillary M2s of the grey mouse lemur to axial loads to mimic one of the most important force components of *in vivo* occlusal loading in mammals (Lin et al., 2013). We found a combination of translation and rotation around the molars' main (i.e. X, Y and Z) axes, although it has to be stressed that the translations in × and y were relatively small and in some experiments even below the effective pixel size (Tables 1 and 3, Supplementary Figure 2). Irrespective of the latter, our results agree with those of Chattah et al., Naveh et al. and Salamati et al. who suggested that teeth show a downward movement with an additional tilting into the mesial direction, see Fig. 4 (Chattah et al., 2009; Naveh et al., 2012b; Salamati et al., 2020). It is likely that under physiological conditions also some off-centre forces occur as it is known that mastication pattern in primates are characterised by variation in bite point throughout a chewing sequence (see (Vinyard et al., 2008)). This caveat notwithstanding, a rotational and downward motion has been said to produce regions within the alveolar bone where compression and tension occur concomitantly and result in lower overall peak stress (Lin et al., 2013). Based on our movement data we identified two main compression areas, namely the inter-radicular furcation and the root tips, both with high apical translations (-Z, Table 3). Corresponding to the thickening of the PDL in the apical region (see above), we observed bulb-shaped root tips with flattened ends in both mandibular and maxillary molars (see Fig. 4). It is possible that this specific root apex morphology increases the surface area and therefore contributes to a load dampening mechanism by dissipating high compression loads. Yet, unlike in the studies by Naveh et al. (Naveh et al., 2012b) and Ho et al. (Ho et al., 2013) we observed a direct tooth-bone contact only in one of our experiments at the inter-radicular furcation area (Supplementary Figure 4). While the maximum load applied was 19 N, which is well below the average maximum recorded bite force for mouse lemur females (36 ± 6 N (Thomas et al., 2015)), it is likely that at higher loads we might have observed more contact areas (see (Naveh et al., 2012b)). This notwithstanding, we propose that the downward-tipping motion in a multi-rooted tooth could be considered a mechanism to increase the distance it has to cover when being pushed into the bony socket, thus delaying tooth-bone contact.

5. Conclusion

This study provides the first insight into the root morphology and whole tooth movement in a non-human primate species, despite some technical limitations. Using synchrotron imaging it was possible to visualize narrowing of the PDL space under load and image the vasculature network within the PDL. Our findings provide further support to existing studies on other non-primate species that the PDL space with its heterogeneous shape and its vasculature distribution is well adapted to sustain occlusal loads. In particular, we identified the bifurcation area and the tooth root tips as important dampening regions within the PDL-alveolar bone interface during tooth movement. In addition, our study provides further support to the notion that a combination of translational and rotational movements may help to dissipate the peak loading within the PDL under load. This mechanism thus likely prevents tooth-bone contact which may eventually lead to tooth fracture or bone (Jang et al., 2018; Naveh et al., 2018; Picton, 1990). Future studies should investigate the effects of physiological blood pressure changes and variable loading conditions to better mimic *in vitro* conditions.

Funding

This research was funded by the Max-Planck-Society. Beam time at the ESRF was granted by the ESRF (proposal LS-2617 to KK) and the DESY (proposal I-20140173 and I-201600017 to ESK).

Data accessibility

The data (8 synchrotron scans) supporting the findings of this study are accessible through the open access data repository of the Max Planck Society (https://doi.org/10.17617/3.57).

Declaration of Competing Interest

The authors declare that they have no known competing financial interests or personal relationships that could have appeared to influence the work reported in this paper.

Acknowledgments

We particularly acknowledge the contribution of our highly esteemed colleague Elke Zimmermann who unexpectedly passed away during the process of finalization of this project. Her scientific contributions to the field of primatology will not be forgotten. We are grateful to Tina Kottek for the preparation and staining of the microscopic sections. Felix Beckmann is thanked for help with the technical implementation of the loading and tomographic experiments at the Helmholtz-Zentrum Geesthacht beamlines at DESY.

Author contributions

KK, ESK, and MB designed the research; AHE, UR, EZ provided specimens; MB conducted the experiments with help from ESK, KK, JH, TMK and AR; AHI and JM contributed to the imaging setup at DESY and the tomographic reconstruction. MB did the 3D image reconstruction and analysed the data; MB, ESK and KK wrote the paper with input from all other co-authors.

Appendix A. Supplementary data

Supplementary data to this article can be found online at https://doi.org/10.1016/j.jsb.2020.107658.

References

Behrend, D.A., 1978. Patterns of tooth displacement in simulated chewing cycles in man. Arch. Oral Biol. 23 (12), 1089–1093. https://doi.org/10.1016/0003-9969(78)90113-9.

Bien, S.M., 1966a. Hydrodynamic Damping of Tooth Movement. J. Dent. Res. 45 (3), 907–914. https://doi.org/10.1177/00220345660450036701.

Bien, S.M., 1966b. Fluid dynamic mechanisms which regulate tooth movement. Adv. Oral Biol. 2, 173–201. https://doi.org/10.1016/b978-1-4832-3118-1.50014-1.

Bosshardt, D.D., Bergomi, M., Vaglio, G., Wiskott, A., 2008. Regional structural characteristics of bovine periodontal ligament samples and their suitability for biomechanical tests. J. Anat. 212 (3), 319–329. https://doi.org/10.1111/j.1469-7580.2008.00856.x.

Buades, A., Coll, B., Morel, J.M., 2005. A non-local algorithm for image denoising, in: Proceedings - 2005 IEEE Computer Society Conference on Computer Vision and Pattern Recognition, CVPR 2005. pp. 60–65. https://doi.org/10.1109/CVPR.2005.38.

Burstone, C.J., Pryputniewicz, R.J., Bowley, W.W., 1978. Holographic measurement of tooth mobility in three dimensions. J. Periodontal Res. 13 (4), 283–294. https://doi.org/10.1111/j.1600-0765.1978.tb00182.x.

Chattah, N.L.T., Kupczik, K., Shahar, R., Hublin, J.J., Weiner, S., 2011. Structure-function relations of primate lower incisors: A study of the deformation of Macaca mulatta dentition using electronic speckle pattern interferometry (ESPI). J. Anat. 218, 87–95. https://doi.org/10.1111/j.1469-7580.2010.01234.x.

Chattah, N.-T., Shahar, R., Weiner, S., 2009. Design Strategy of Minipig Molars Using Electronic Speckle Pattern Interferometry: Comparison of Deformation under Load between the Tooth-Mandible Complex and the Isolated Tooth. Adv. Mater. 21 (4), 413–418. https://doi.org/10.1002/adma.200801187.

Chazeau, C., Marchal, J., Hackert, R., Perret, M., Herrel, A., 2013. Proximate determinants of bite force capacity in the mouse lemur: Bite force in mouse lemurs. J. Zool. 290 (1), 42–48. https://doi.org/10.1111/jzo.12011.

Chiba, M., Yamane, A., Ohshima, S., Komatsu, K., 1990. In vitro measurement of regional differences in the mechanical properties of the periodontal ligament in the rat mandibular incisor. Arch. Oral Biol. 35 (2), 153–161. https://doi.org/10.1016/0003-9969(90)90177-C.

Coolidge, E.D., 1937. The Thickness of the Human Periodontal Membrane. J. Am. Dent. Assoc. Dent. Cosm. 24 (8), 1260–1270. https://doi.org/10.14219/jada.archive.1937.0229.

Dalstra, M., Cattaneo, P.M., Laursen, M.G., Beckmann, F., Melsen, B., 2015. Multi-level synchrotron radiation-based microtomography of the dental alveolus and its consequences for orthodontics. J. Biomech. 48 (5), 801–806. https://doi.org/10.1016/j.jbiomech.2014.12.014.

Dammhahn, M., Kappeler, P.M., 2008. Comparative Feeding Ecology of Sympatric Microcebus berthae and M. murinus. Int. J. Primatol. 29 (6), 1567–1589. https://doi.org/10.1007/s10764-008-9312-3.

Erko, M., Younes-Metzler, O., Rack, A., Zaslansky, P., Young, S.L., Milliron, G., Chyasnavichyus, M., Barth, F.G., Fratzl, P., Tsukruk, V., Zlotnikov, I., Politi, Y., 2015. Micro- and nano-structural details of a spider's filter for substrate vibrations: relevance for low-frequency signal transmission. J. R. Soc. Interface 12 (104), 20141111. https://doi.org/10.1098/rsif.2014.1111.

Haibel, A., Beckmann, F., Dose, T., Herzen, J., Ogurreck, M., Müller, M., Schreyer, A., 2010. Latest developments in microtomography and nanotomography at PETRA III. Powder Diffr. 25 (2), 161–164. https://doi.org/10.1154/1.3428364.

Haibel, A., Ogurreck, M., Beckmann, F., Dose, T., Wilde, F., Herzen, J., Müller, M., Schreyer, A., Nazmov, V., Simon, M., Last, A., Mohr, J., 2010b. Micro- and nano-tomography at the GKSS Imaging Beamline at PETRA III, in: Stock, S.R. (Ed.), Developments in X-Ray Tomography VII. International Society for Optics and Photonics, p. 78040B. https://doi.org/10.1117/12.860852.

Hildebrand, T., Rüegsegger, P., 1997. A new method for the model-independent assessment of thickness in three-dimensional images. J. Microsc. 185, 67–75. https://doi.org/10.1046/j.1365-2818.1997.1340694.x.

Hipp, A., 2019. High-resolution grating-based phase-contrast imaging for synchrotron radiation sources.

Hipp, A., Herzen, J., Hammel, J.U., Lytaev, P., Schreyer, A., Beckmann, F., 2016. Single-grating interferometer for high-resolution phase-contrast imaging at synchrotron radiation sources. In: Stock, S.R., Müller, B., Wang, G. (Eds.), Developments in X-Ray Tomography X. International Society for Optics and Photonics, p. 996718. https://doi.org/10.1117/12.2237582.

Ho, S.P., Kurylo, M.P., Grandfield, K., Hurng, J., Herber, R.-P., Ryder, M.I., Altoe, V., Aloni, S., Feng, J.Q., Webb, S., Marshall, G.W., Curtis, D., Andrews, J.C., Pianetta, P., 2013. The plastic nature of the human bone–periodontal ligament–tooth fibrous joint. Bone 57 (2), 455–467. https://doi.org/10.1016/j.bone.2013.09.007.

Ho, S.P., Marshall, S.J., Ryder, M.I., Marshall, G.W., 2007. The tooth attachment mechanism defined by structure, chemical composition and mechanical properties of collagen fibers in the periodontium. Biomaterials 28 (35), 5238–5245. https://doi.org/10.1016/j.biomaterials.2007.08.031.

Horn, B.K.P., 1987. Closed-form solution of absolute orientation using unit quaternions. J. Opt. Soc. Am. A 4 (4), 629. https://doi.org/10.1364/JOSAA.4.000629.

Imamura, N., Nakata, S., Nakasima, A., 2002. Changes in periodontal pulsation in relation to increasing loads on rat molars and to blood pressure. Arch. Oral Biol. 47 (8), 599–606. https://doi.org/10.1016/S0003-9969(02)00041-9.

Jang, A.T., Chen, L., Shimotake, A.R., Landis, W., Altoe, V., Aloni, S., Ryder, M., Ho, S.P., 2018. A Force on the Crown and Tug of War in the Periodontal Complex. J. Dent. Res. 97 (3), 241–250. https://doi.org/10.1177/0022034517744556.

Jang, A.T., Merkle, A.P., Fahey, K.P., Gansky, S.A., Ho, S.P., 2015. Multiscale biomechanical responses of adapted bone–periodontal ligament–tooth fibrous joints. Bone 81, 196–207. https://doi.org/10.1016/j.bone.2015.07.004.

Jenatschke, F., 1975. Elektronische Zahnbeweglichkeitsmessungen an oberen Incisivi bei Kindern mit Protrusion. Fortschr. Kieferorthop. 36 (2), 189–200. https://doi.org/10.1007/BF02171644.

Jozat, R., 1933. Changes in the Periodontal Tissues Caused by Changes in Occlusion. Dtsch, Zahnärztliche Wochenschrift, p. 36.

Kawarizadeh, A., Bourauel, C., Jäger, A., 2003. Experimental and numerical determination of initial tooth mobility and material properties of the periodontal ligament in rat molar specimens. Eur. J. Orthod. 25, 569–578. https://doi.org/10.1093/ejo/25.6.569.

Kindlová, M., Matena, V., 1962. Blood Vessels of the Rat Molar. J. Dent. Res. 41 (3), 650–660. https://doi.org/10.1177/00220345620410031801.

Klein, A., 1928. Systematische Untersuchungen über die Periodontalbreite. Z. Stomatol. 26 (6), 417–439.

Lautner, S., Lenz, C., Hammel, J.U., Moosmann, J., Kühn, M., Caselle, M., Vogelgesang, M., Kopmann, A., Beckmann, F., 2017. Using SRuCT to define water transport capacity in Picea abies, in: Müller, B., Wang, G. (Eds.), Developments in X-Ray Tomography XI. SPIE, p. 53. https://doi.org/10.1117/12.2287221.

Kupczik, K., Dean, M.C., 2008. Comparative observations on the tooth root morphology of *Gigantopithecus blacki*. J. Hum. Evol. 54, 196–204. https://doi.org/10.1016/j.jhevol.2007.09.013.

Le Cabec, A., Tang, N.K., Ruano Rubio, V., Hillson, S., 2019. Nondestructive adult age at death estimation: Visualizing cementum annulations in a known age historical human assemblage using synchrotron X-ray microtomography. Am. J. Phys. Anthropol. 168 (1), 25–44. https://doi.org/10.1002/ajpa.23702.

LeBlanc, A.R.H., Brink, K.S., Whitney, M.R., Abdala, F., Reisz, R.R., 2018. Dental ontogeny in extinct synapsids reveals a complex evolutionary history of the mammalian tooth attachment system. Proc. R. Soc. B Biol. Sci. 285 (1890), 20181792. https://doi.org/10.1098/rspb.2018.1792.

LeBlanc, A.R.H., Reisz, R.R., Brink, K.S., Abdala, F., 2016. Mineralized periodontia in extinct relatives of mammals shed light on the evolutionary history of mineral homeostasis in periodontal tissue maintenance. J. Clin. Periodontol. 43 (4), 323–332. https://doi.org/10.1111/jcpe.12508.

Lin, J.D., Özcoban, H., Greene, J.P., Jang, A.T., Djomehri, S.I., Fahey, K.P., Hunter, L.L., Schneider, G.A., Ho, S.P., 2013. Biomechanics of a bone–periodontal ligament–tooth fibrous joint. J. Biomech. 46 (3), 443–449. https://doi.org/10.1016/j.jbiomech.2012.11.010.

Lösel, P., Heuveline, V., 2016. Enhancing a diffusion algorithm for 4D image segmentation using local information, in: Styner, M.A., Angelini, E.D. (Eds.), Medical Imaging 2016: Image Processing. p. 97842L. https://doi.org/10.1117/12.2216202.

Luke, D.A., 1992. The structure and functions of the dentogingival junction and periodontal ligament. Br. Dent. J. 172 (5), 187–190. https://doi.org/10.1038/sj.bdj.4807818.

Manly, R.S., Yurkstas, A., Reswick, J.B., 1951. An Instrument for Measuring Tooth Mobility. J. Periodontol. 22 (3), 148–155. https://doi.org/10.1902/jop.1951.22.3.148.

McDonald, F., 2009. Oral anatomy, histology and embryology, 4th edition (2009). Eur. J. Orthod. 31 (4), 457–458. https://doi.org/10.1093/ejo/cjp045.

Miura, H., Hasegawa, S., Okada, D., Ishihara, H., 1998. The measurement of physiological tooth displacement in function. J. Med. Dent. Sci. 45, 103–115. https://doi.org/10.11480/jmds.450206.

Mühlemann, H.R., 1951. Periodontometry, a method for measuring tooth mobility. Oral Surg. Oral Med. Oral Pathol. 4 (10), 1220–1233. https://doi.org/10.1016/0030-4220(51)90080-1.

Murrell, E.F., Yen, E.H.K., Johnson, R.B., 1996. Vascular changes in the periodontal ligament after removal of orthodontic forces. Am. J. Orthod. Dentofac. Orthop. 110 (3), 280–286. https://doi.org/10.1016/S0889-5406(96)80012-6.

Nanci, A., Bosshardt, D.D., 2006. Structure of periodontal tissues in health and disease. Periodontol 2000 40 (1), 11–28. https://doi.org/10.1111/j.1600-0757.2005.00141.x.

Naveh, G.R.S., Brumfeld, V., Shahar, R., Weiner, S., 2013. Tooth periodontal ligament: Direct 3D microCT visualization of the collagen network and how the network changes when the tooth is loaded. J. Struct. Biol. 181 (2), 108–115. https://doi.org/10.1016/j.jsb:2012.10.008.

Naveh, G.R.S., Foster, J.E., Silva Santisteban, T.M., Yang, X., Olsen, B.R., 2018. Nonuniformity in ligaments is a structural strategy for optimizing functionality. Proc. Natl. Acad. Sci.USA 115 (36), 9008–9013. https://doi.org/10.1073/pnas.1807324115.

Naveh, G.R.S., Lev-Tov Chattah, N., Zaslansky, P., Shahar, R., Weiner, S., 2012a. Tooth–PDL–bone complex: Response to compressive loads encountered during mastication – A review. Arch. Oral Biol. 57 (12), 1575–1584. https://doi.org/10.1016/j.archoralbio.2012.07.006.

Naveh, G.R.S., Shahar, R., Brumfeld, V., Weiner, S., 2012b. Tooth movements are guided by specific contact areas between the tooth root and the jaw bone: A dynamic 3D microCT study of the rat molar. J. Struct. Biol. 177 (2), 477–483. https://doi.org/10.1016/j.jsb:2011.11.019.

Naveh, G.R.S., Weiner, S., 2015. Initial orthodontic tooth movement of a multirooted tooth: a 3D study of a rat molar. Orthod. Craniofac. Res. 18 (3), 134–142. https://doi.org/10.1111/ocr.12066.

NG, G.C., Walker, T.W., Zingg, W., Burke, P.S., 1981. Effects of tooth loading on the periodontal vasculature of the mandibular fourth premolar in dogs. Arch. Oral Biol. 26 (3), 189–195. https://doi.org/10.1016/0003-9969(81)90129-1.

Nikolai, R.J., 1996. Rigid-body kinematics and single-tooth displacements. Am. J. Orthod. Dentofac. Orthop. 110 (1), 88–92. https://doi.org/10.1016/S0889-5406(96)70092-6.

Nikolaus, A., Currey, J.D., Lindtner, T., Fleck, C., Zaslansky, P., 2017. Importance of the variable periodontal ligament geometry for whole tooth mechanical function: A validated numerical study. J. Mech. Behav. Biomed. Mater. 67, 61–73. https://doi.org/10.1016/j.jmbbm.2016.11.020.

Pal, A., Chen, L., Yang, L., Yang, F., Meng, B., Jheon, A.H., Ho, S.P., 2017. Micro-anatomical responses in periodontal complexes of mice to calibrated orthodontic forces on the crown. Orthod. Craniofac. Res. 20, 100–105. https://doi.org/10.1111/ocr.12172.

Persson, R., 1981. Assessment of tooth mobility using small loads. III. Effect of periodontal treatment including a gingivectomy procedure. J. Clin. Periodontol. 8 (1), 4–11. https://doi.org/10.1111/j.1600-051X.1981.tb02018.x.

Picton, D.C.A., 1990. Tooth mobility–an update. Eur. J. Orthod. 12 (1), 109–115. https://doi.org/10.1093/ejo/12.1.109.

Picton, D.C.A., 1963. Vertical movement of cheek teeth during biting. Arch. Oral Biol. 8 (2), 109–118. https://doi.org/10.1016/0003-9969(63)90048-7.

Picton, D.C.A., Davies, W.I.R., 1967. Dimensional changes in the periodontal membrane of monkeys (Macaca irus) due to horizontal thrusts applied to the teeth. Arch. Oral Biol. 12 (12), 1635–1643. https://doi.org/10.1016/0003-9969(67)90197-5.

Pini, M., Zysset, P.h., Botsis, J., Contro, R., 2004. Tensile and compressive behaviour of the bovine periodontal ligament. J. Biomech. 37 (1), 111–119. https://doi.org/10.1016/S0021-9290(03)00234-3.

Preissecker, O., 1931. Changes in the Periodontal Tissues by Experimental Decrease of Occlusal Stress. Z. Stomatol. (1921). 29, 442.

Rack, A., Stroebel, J., Rack, T., Dabin, Y., Knabe, C., Stiller, M., Coan, P., Bleuet, P., 2020. TomoPress—In Situ Synchrotron-Based Microtomography under Axial Load. Instruments 4, 11. https://doi.org/10.3390/instruments4020011.

Radlanski, R.J., 2011. Orale Struktur- und Entwicklungsbiologie. Orale Struktur- und Entwicklungsbiologie, Quintessenz-Verl.

Salamati, A., Chen, J., Herring, S.W., Liu, Z.-J., 2020. Functional tooth mobility in young pigs. J. Biomech. 104, 109716. https://doi.org/10.1016/j.jbiomech.2020.109716.

Sanctuary, C., 2003. Experimental Investigation of the Mechanical Behaviour and Structure of the Bovine Periodontal Ligament 2902. https://doi.org/10.5075/epfl-thesis-2902.

Schroeder, H.E., 1986. Schroeder, Hubert E., Springer Berlin Heidelberg. Springer Berlin Heidelberg, Berlin, Heidelberg. https://doi.org/10.1007/978-3-642-71261-6.

SIEBERT, G., Siebert, G., 1981. Recent results concerning physiological tooth movement and anterior guidance. J. Oral Rehabil. 8 (6), 479–493. https://doi.org/10.1111/j.1365-2842.1981.tb00523.x.

Slatter, J.M., Picton, D.C.A., 1972. The effect on intrusive tooth mobility of noradrenaline injected locally in monkeys. J. Periodontal Res. 7 (2), 144–150. https://doi.org/10.1111/j.1600-0765.1972.tb00639.x.

Smith, R.J., Burstone, C.J., 1984. Mechanics of tooth movement. Am. J. Orthodontics 85 (4), 294–307. https://doi.org/10.1016/0002-9416(84)90187-8.

Storey, E., 1973. The nature of tooth movement. Am. J. Orthod. 63 (3), 292–314. https://doi.org/10.1016/0002-9416(73)90353-9.

Swindler, D.R., 2002. Primate Dentition: An Introduction to the Teeth of Non-human Primates . Cambridge Studies in Biological and Evolutionary Anthropology, Volume 32 . By Daris R Swindler ; illustrated by , Robert M George. Cambridge and New York: Cambridge University Pres, The Quarterly Review of Biology. Cambridge University Press. https://doi.org/10.1086/374488.

Tafforeau, P., Zermeno, J.P., Smith, T.M., 2012. Tracking cellular-level enamel growth and structure in 4D with synchrotron imaging. J. Hum. Evol. 62 (3), 424–428. https://doi.org/10.1016/j.jhevol.2012.01.001.

Thomas, P., Pouydebat, E., Hardy, I., Aujard, F., Ross, C.F., Herrel, A., 2015. Sexual dimorphism in bite force in the grey mouse lemur: Lemur bite force sexual dimorphism. J. Zool. 296 (2), 133–138. https://doi.org/10.1111/jzo.12225.

Vinyard, C.J., Wall, C.E., Williams, S.H., Hylander, W.L., 2008. Patterns of variation across primates in jaw-muscle electromyography during mastication, in: Integrative and Comparative Biology. pp. 294–311. https://doi.org/10.1093/icb/icn071.

Wills, D.J., Picton, D.C.A., Davies, W.I.R., 1976. A study of the fluid systems of the periodontium in macaque monkeys. Arch. Oral Biol. 21 (3), 175–185. https://doi.org/10.1016/0003-9969(76)90127-8.

Willumeit-Römer, R., Moosmann, J., Zeller-Plumhoff, B., Florian Wieland, D.C., Krüger, D., Wiese, B., Wennerberg, A., Peruzzi, N., Galli, S., Beckmann, F., Hammel, J.U., 2018. Visualization of implant failure by synchrotron tomography, in: Minerals, Metals and Materials Series. Springer, Cham, pp. 275–284. https://doi.org/10.1007/978-3-319-72526-0_25.

Yoshida, N., Jost-Brinkmann, P.-G., Koga, Y., Mimaki, N., Kobayashi, K., 2001. Experimental evaluation of initial tooth displacement, center of resistance, and center of rotation under the influence of an orthodontic force. Am. J. Orthod. Dentofac. Orthop. 120 (2), 190–197. https://doi.org/10.1067/mod.2001.115036.

Zablocki Thomas, P.B., Karanewsky, C.J., Pendleton, J.L., Aujard, F., Pouydebat, E., Herrel, A., 2018. Drivers of in vivo bite performance in wild brown mouse lemurs and a comparison with the grey mouse lemur. J. Zool. 305 (3), 180–187. https://doi.org/10.1111/jzo.12550.

Zanoni, J.N., Lucas, N.M., Trevizan, A.R., Souza, I.D.S., 2013. Histological evaluation of the periodontal ligament from aged wistar rats supplemented with ascorbic acid. An. Acad. Bras. Ciênc. 85 (1), 327–335. https://doi.org/10.1590/S0001-37652013005000003.